A climatology of the nighttime thermospheric winds over Sutherland, South Africa ☆

Taiwo T. Ojo[a,b], Zama T. Katamzi-Joseph[a,b], Kristina T. Chu[c], Matthew A. Grawe[d], Jonathan J. Makela[c]

[a] *South African National Space Agency (SANSA) Space Science, P.O. Box 32, Hermanus 7200, South Africa*
[b] *Department of Physics and Electronics, Rhodes University, Eastern Cape, Grahamstown 6139, South Africa*
[c] *Department of Electrical and Computer Engineering, University of Illinois at Urbana-Champaign, Urbana, Illinois, USA*
[d] *Johns Hopkins University, Applied Physics Laboratory, Laurel, Maryland, USA*

Abstract

We present a climatology of nighttime thermospheric neutral winds between February 2018 and January 2019 measured by a Fabry-Perot interferometer (FPI) located in Sutherland, South Africa (32.2°S, 20.48°E; geomagnetic latitude: 40.7°S). This FPI measures the nighttime oxygen airglow emission at 630.0 nm, which has a peak emission at an altitude of roughly 250 km. The annual meridional and zonal winds at this location vary between -100 and 120 m/s and show typical midlatitude nocturnal and seasonal variations. During local summer months (December-February), the meridional wind is predominantly equatorward from dusk to predawn. However, during the winter months, the meridional wind is poleward from dusk, turns equatorward around midnight, and either remains in this direction for the rest of the night (June) or turns poleward again just before dawn (July and August). The zonal wind velocity is generally eastward during the evening until just before midnight, changing westward post-midnight. The zonal wind peaks at higher velocities during the winter months compared to the summer months. The eastward-to-westward transition occurs later during the winter months compared to the summer months. We compare results from HWM14 with the FPI measurements and find a better agreement between FPI measured

Email address: princetaiwoojo1@gmail.com, tojo@sansa.org.za (Taiwo T. Ojo)

winds and HWM14 modeled winds for the meridional component compared to the zonal component. In addition, the HWM14 zonal wind consistently peaked several hours ($\sim$ 3 hours) prior to the measured wind. Furthermore, the HWM14-modeled eastward-to-westward transitions times were a couple of hours ($\sim$ 2 hours) earlier during the months of November to January creating what looks like a phase shift compared to the measured wind. This phase shift was apparent in all months and we suggest this can be attributed to a phase shift of the terdiurnal tide between the model and measurements.

Keywords:
Nighttime thermospheric winds, FabryPerot interferometer (FPI),
Horizontal wind model (HWM14)

---

1. Introduction

Neutral winds in Earth's thermosphere are **primarily** generated by pressure gradients due to changes in temperature that are mainly driven by solar heating (Brum et al., 2012). The dynamics in the upper atmosphere are greatly influenced by neutral winds as they play a crucial role in the dynamics of the F region ionosphere as well as in the generation of electric fields and currents, instabilities, and Joule heating (Rees, 1995; Heelis, 2004).

Despite their significant contribution to ionospheric dynamics, themospheric neutral winds are generally insufficiently sampled parameters in the Earth's upper atmosphere. Most of the climatological studies of these neutral parameters have been conducted over the American and Asian longitudinal sectors as well as the European mid-to-high latitude regions (e.g., Fisher et al., 2015; Yu et al., 2014; Xu et al., 2019). However over the past decade, there have been several FPI deployments in the African continent making it possible to study neutral winds over the Africa sector. One of the first studies to report wind climatology over the African continent was by Fisher et al. (2015) using FPI measurements over Morocco, north Africa. Subsequent studies have been conducted by Tesema et al. (2017), Kaab et al. (2017) and Sivla et al. (2019), over Ethiopia, Morocco and Nigeria respectively. Generally the winds trends over these locations are comparable to those of similar latitude regions in other longitudinal sectors although there are some discrepancies.

Still, there has not been a detailed climatological study of neutral winds over the southern midlatitude region in Africa due to lack of observations. This has changed with the deployment of an FPI in Sutherland (32.2°S, 20.48°E; geomagnetic latitude: 40.7°S) in January 2018. Therefore this paper presents the first results of seasonal variations of the horizontal winds over this location using FPI observations during the period of February 2018 to January 2019. We also validate meridional and zonal winds in this sector provided by the horizontal wind model (HWM14), an empirical model of the horizontal neutral wind in the upper atmosphere (Drob et al., 2015).

2. Instrumentation

The Fabry-Perot interferometer (FPI) is a widely-used optical instrument for probing the thermosphere to measure thermospheric neutral winds (e.g., Bamgboye and McClure, 1982, Spencer et al., 1982; Sahai et al., 1992; McLandress et al., 1996; Emmert et al., 2002; Fejer et al., 2002; Meriwether, 2006; Emmert et al., 2006; Häusler et al., 2007; Brum et al., 2012; Makela et al., 2013; Yu et al., 2014; Fisher et al., 2015). The FPI is designed to measure the spectral line shape of the airglow emmission at a specific wavelength, for example 557.7 or 630.0 nm. In this study the FPI measures the redline emission at 630.0 nm, which is produced through the dissociative recombination of O_2^+ (Link and Cogger, 1988). The nighttime redline emission naturally occurs at an altitude of approximately 250 km. By measuring the Doppler shift of this emission at high spectral resolution, the FPI can be used to estimate line-of-sight neutral wind velocities.

The FPI used in this study is designed with an etalon having an air gap of 15 mm and reflectivity of $\sim 77\%$. A 1 nm full width half maximum narrow band interference filter centered at 630.0 nm with $\sim 55\%$ transmission is placed in the optical path before the etalon to isolate the redline emission from other background emissions. The interference pattern created by the etalon is then imaged using an objective lens onto a 13.3×13.3 mm Andor CCD. This CCD has 1024×1024 pixels (binned to 512×512) and is thermoelectrically cooled to below -60°C to reduce the effects of dark current (Harding, 2017). A dual-mirror sky-scanning system, driven by a smart motor on each axis, sits directly above the optics and allows observations of the

sky in any direction by rotating in the elevation and the azimuth planes.

A typical observing set up for the Sutherland FPI deployment observes the zenith direction, followed by each of the four cardinal directions (north, east, south and west) at an elevation angle of 45°. **A typical observing cycle takes $\sim$ 27 minutes**. Each observation of the sky is followed by an observation of a frequency-stabilized HeNe laser to monitor the parameters of the instrument. This observation strategy is regarded as "cardinal mode" and allows both meridional and zonal components to be extracted from the measurements.

A cloud sensor has also been installed alongside the FPI to provide information on the viewing conditions. The sensor measures the sky temperature and the ambient temperature and reports the difference between the two. When available, this information is used to remove observations from the analysis that were taken during cloudy conditions. The empirically chosen cutoff temperature for detecting cloud cover is -20°C (Fisher et al., 2015).

3. Data Analysis

Data are analyzed based on the method described in Harding et al. (2014). This method results in estimates of wind values, along with estimates of uncertainties. For the results presented here, we deduced the zero-wind reference needed for absolute estimates of wind velocities by using observations of the frequency-stabilized HeNe combined with observations made towards the zenith direction assuming that the average vertical wind over the night is zero. To ensure only high-quality data for quiet geomagnetic conditions are used in the analysis, wind values outside the range of (-200; 200) m/s were considered as unrealistic and therefore discarded. Also, wind and temperature measurements with uncertainties greater than 25 m/s and 50 K respectively were discarded. Furthermore, in this study we compare the measurements to HWM14 which is a quiet time model therefore, **any night with Kp $>$ 3 is removed while calculating the monthly averages**, discussed below.

FPI winds measurements that remain after the data quality check process taken in a given month are sorted into 30-minutes local time bins for each cardinal look direction. Any small temporal gradients will be averaged out in

this binning process. For each time bin in each month, a statistical analysis was done by computing the weighted mean and sample standard deviation (variability). The weighted mean for x, where x is the set of neutral winds measurements was computed as:

$$\tilde{x} = \frac{\sum_i x_i w_i}{\sum_i w_i} \tag{1}$$

where $w_i = \frac{1}{\sigma_i^2}$ is the weight and σ_i is the uncertainty of the measurements. The sample standard deviation was computed as:

$$s = \sqrt{\frac{1}{n-1}\sum_i (x_i - \tilde{x})^2} \tag{2}$$

where n is the number of samples in x. When seasonal variation is discussed, seasons are categorised as summer (December-February), autumn (March-May), winter (June-August) and spring (September-November).

4. Results

Figure 1 shows the number of nights having FPI observations, the number of quiet nights, and the number of used nights per month. Figure 2 presents seanonal occurrence of solar flux (F10.7), Ap index and geomagnetic activity values (Ap and Kp indices). Also, the solar and geomagnetic activies are low throughout this period; solar flux ranged between 75 and 85 solar flux units (sfu) where 1 sfu = 10^{-22} W/m^2/Hz, and Kp and Ap indices were less than 4 and 25, respectively. Each figure is plotted in solar local time (SLT), which defines noon as the time when the sun is the highest in the sky and can be mathematically calculated using.

$$SLT = t_{UT} - \theta \frac{24}{360^\circ} \tag{3}$$

where SLT is the solar local time (hours), t_{UT} is the universal time (hours), and θ is the longitude our FPI site.

4.1 Meridional and Zonal Wind Monthly Averages

The contour plot in Figure 3 (top) show the monthly average of the meridional wind between February 2018-January 2019. The meridional wind average over Sutherland, South Africa, exhibits a predominantly diurnal variation being equatorward at night. The annual behavior being more equatorward during the summer and poleward during the winter. Furthermore, the average of this component does not show a clear semi-annual variation but just an asymmetric annual behavior. The zonal wind average also exhibits predominantly diurnal variation is more eastward during the winter and westward during the summer for the entire night, as shown in Figure 3 (bottom). In addition, the average of this component does not show a clear semi-annual variation but just an asymmetric annual behavior.

Monthly averages of the FPI meridional and zonal winds measurement made between February 2018 and January 2019 are presented in Figures 4 and 5, respectively. Also plotted are winds provided by the HWM14 model (blue curves). Generally, for most months (March-November) the observed meridional wind is poleward (southward; negative) after dusk, turning equatorward and remaining in this direction for the rest of the night or turning poleward again a couple of hours before dawn. The poleward-to-equatorward transition time is between 21:00 and 02:00 SLT for May-November, and between 04:00 and 06:00 SLT for March and April. During February the measured meridional wind is equatorward until 04:00 SLT when it turns poleward, while in December and January wind flows equatorward only. For most of the months (with the exception of May-August) an increase in measured meridional wind is observed from the early evening to reach a premidnight peak of $\sim$ 70-90 m/s before decreasing and turning poleward. The peak is observed post midnight for the months of May-August. This indicates that the peak of the equatorward wind shifts from around midnight in the summer months to postmidnight in winter months. Also, during the summer months the measured meridional wind is only or mostly equatorward. For the winter months (May-July) it is predominantly poleward (negative) during the evening period between 19:00 and 21:00 SLT and changes to poleward at midnight. This is followed by a gradual decrease in the amplitude of meridional wind and a poleward reversal before dawn. While this wind direction

change is also observed during spring and autumn months, the switch in direction occurs much later in winter, at around midnight, compared to around 20:30-21:00 SLT during the months of March, April and September.

In comparison to the measured winds, the HWM14 model generally captures a similar wind trend for the months of October through February i.e., HWM14 model predicted equatorward wind for all or most observed hours of the nights. Also, similar to the FPI, the HWM14 results during the months of April-September show a poleward wind in the early evening which later switches equatorward. Furthermore, the amplitudes of the HWM14 meridional winds during the winter months (May-August) are smaller than summer months (November-February) in general agreement with the measurements.

However, when looking at the details of the comparison there are also several discrepancies between the data and model in regards to the time of wind direction transition, the amplitude of wind, and the time when the peak of equatorward wind occurs. For instance, the HWM14 model overestimates the meridional winds by $\sim$ 20 m/s in the summer months, mostly at the beginning of the night. Also, the model predicts the peak of the equatorial meridional wind much earlier during April, August-January, while it occurs later during the months of June-July compared to measurements from the FPI. The time difference between the peaks in HWM14 and FPI measurements can vary between 2 hours (April) and 5 hours (August). These sort of discrepancies are perhaps not terribly surprising given that the general construction of HWM14 lacks data from the Africa region.

Turning to the zonal winds, the direction of the measured zonal wind presented in Figure 5 is predominantly eastward (positive) before midnight, and westward (negative) post-midnight until predawn. For all months, an increase in zonal wind is observed from the early evening to reach a premidnight peak of $\sim$ 90-120 m/s before decreasing and turning westward. The amplitude of the winds is larger during the winter months ($\sim$ 120 m/s; July and August) than the summer months ($\sim$ 60 m/s; February and December). This peak occurred much earlier during the winter months ($\sim$ 120 m/s; July and August) compared to the summer months ($\sim$ 60 m/s; February and December). The eastward-to-westward transition time is between 01:30 SLT and 02:00 SLT for the months of November-February, and between 04:00 and 05:30 SLT for months March-October. This indicates that the transition

time occurs later during the winter season (May-August) compared to summer (December-February). For September, October, January and February, a peak in the westward wind is observed around 23:00-02:00 SLT. Furthermore, the zonal wind around 19:00-22:00 SLT during spring and autumn (e.g. March, September, October and November) has lower values compared to the same time during winter and summer months (e.g. January and February).

Similar to the FPI measured zonal wind trends, the HWM14 model predicts eastward zonal wind during the evening hours prior to midnight (± 3 hours) before switching to westward for the rest of the night. The eastward-to-westward transition time predicted by the HWM14 model is similar to those measured by the FPI for most months, e.g. February-October. However the model estimates a significantly earlier transition time for the months of November-January, with a discrepancy as large as ~ 2 hours, creating what looks like a phase shift between the model and data. Between March and November the model disagrees with the observations from early hours of the evening (19:00 and 23:00 SLT), predicting eastward wind that is about $\sim$ 30 m/s faster than the FPI measurements. Furthermore, the peak of the eastward wind is predicted much earlier in time by the model compared to the observations, with a difference between the peak in HWM14 and FPI as large as ~ 3 hours (e.g., March-October).

4.2 Terdiurnal tides in HWM model

We investigate the apparent phase shift between the measured zonal wind and that obtained from the HWM14 model by first extracting and examining the tidal components. This is motivated by the observed shift in timing of the zero wind crossing and peak zonal wind between measurements and model, presented above. Following the method described in Chu (2019), a least squares fitting procedure was implemented to determine the contributions from the diurnal, semidiurnal and terdiurnal tides to the overall thermospheric wind in the model at 250-km altitude, using the relation below:

$$f = A_i sin(\omega_1 t + \gamma_i) + A_i sin(\omega_2 t + \gamma_i) + A_i sin(\omega_3 t + \gamma_i) + B \qquad (4)$$

where $\omega_1 = 2\pi/24$, $\omega_2 = 2\pi/12$, $\omega_3 = 2\pi/8$ are diurnal, semidiurnal and terdiurnal components, respectively, t represents time in hours, A_i represents the amplitudes of the respective tidal components, γ_i represents the phases (in radians) of the tidal components ($i = 1, 2, 3$) and B is used to account for a non-zero mean signal.

As is evident in Figure 5, there is an apparent phase shift present in the zonal winds that offsets the peak seen in HWM to be approximately 2-3 hours earlier than that shown by the data. Because factors influencing the terdiurnal tide occur much more locally than those influencing the diurnal or semidiurnal components (Fisher et al., 2015; Jiang et al., 2018; Chu, 2019), we can assume that changing characteristics of the terdiurnal tide will only affect the winds close to this site. Coupled with the relative lack of ground-based data from southern Africa used in the construction of HWM, it is not surprising, then, that the match between the data and model are not as good as in other sectors in which more ground-based data were available. To investigate this we decompose the HWM modeled winds into differing tidal components and adjust the properties of the terdiurnal tide to see if through modifying that component alone, a better data-model match can be found.

Since the amplitude of the peak zonal wind estimated by HWM matches the data relatively well, we focus on only shifting the phase of the terdiurnal tide to create a better match between model and data. For each month, we compared the averaged nightly winds obtained from FPI measurements and binned and averaged winds from HWM, following the methodology described in Section 3. For each monthly average, we used the Taylor diagram (Taylor, 2001) to quantify the standard deviation σ_r of the data r, σ_d the standard deviation of model d, and the correlation R_r between the data and model. To keep the geometry the same, we used a normalized Taylor diagram (in which the standard deviation of the model is normalized to the standard deviation of the data). The Taylor diagram provides a straightforward way to investigate differences between data and model. An example is given in Figure 6. Each data-model comparison is plotted on the polar coordinate system. A model that perfectly matches the data would be located at the intersection between the $\sigma_r = 1$ arc and the x-axis (indicating $R_r = 1$). The RMS differences between model and data are denoted by the gray circles, centered on the point of perfect agreement. Models whose "shape" matches the data will lie close to the x-axis. Models which captures the variance of

the data will lie close to the $\sigma_r = 1$ arc.

To investigate how much of the discrepancy between data and model seen in Figure 5 could be explained by an incorrect estimate of the phase of the terdiurnal tide, we first decompose the HWM into tidal components by fitting the model's monthly average to Equation 4. The phase of the terdiurnal tide, γ_3 is shifted and the wind is then reconstructed (again, using Equation 4). We step through phase shifts and compare the reconstruction to data, calculating the corresponding (σ_d, R_d) and plot each comparison on the Taylor diagram. An example is shown in Figure 6. Each different hypothesized phase shift is shown by a different color. Through this exercise, we can identify the phase shift that maximized correlation (R_d), matched the normalized stanadard deviation (σ_d), or minimized RMS error (D). The RMS error is calculated as:

$$D = \sqrt{\sigma_r^2 + \sigma_d^2 - 2\sigma_r\sigma_d R_d} \tag{5}$$

For the example presented in Figure 6b, we show the reconstructed wind. The results shown in purple, which maximized the correlation is seen to match quite well in shape and amplitude at the peak. However, as the peak falls off after 21:00 SLT there is an amplitude difference between the model and the data (shown in black). The result shown in green point shows that the amplitude maximum matches fairly well and there is less of the amplitude discrepancy as the peak falls off than there is for the best correlation case, but the peak timing is quite different and remains almost identical to the original model output. Finally, the reconstruction corresponding to the phase that gives the smallest D (shown in blue) balances the correct peak timing and general shape from the best correlation case with the fall off behavior influenced slightly by the best standard deviation case. Using the results that minimize D instead of those that maximize the correlation R allows us to avoid cases where the best correlation case might result in a model output that is shifted so much that there is a large amplitude difference between model and data.

Figure 7 clearly shows the improvements in data-model comparisons found

by allowing for a phase shift in only the terdiurnal tidal component estimated from HWM14. During January and February the improvement in the RMS error (D) ranges are 1.82 to 7.49 but during local winter there is larger improvement ranging from 6.62 to 21.76. The largest improvement comes in November (improvement of 23.03) and December (improvement of 25.59) as shown in Table 1. For all months, we are able to improve both the standard deviation and the correlation of the original HWM output; comparing the original and modified HWM wind results with the data, for almost all months the modified HWM wind represents the data much more closely. In addition, the apparent phase shift between the peak wind in the data and HWM output has been greatly reduced. Shifting the terdiurnal phase is particularly effective for March-July, but in August-November the shift with the smallest D results in shifting the predicted peak winds approximately an hour after the peak wind in the data. It also causes the peak amplitude to be overestimated, particularly in August and September, where it is overestimated by almost 30 m/s. It is also important to note that for February, shifting the terdiurnal tide was unsuccessful at correcting the apparent phase shift between data and HWM. This indicates that there is still something that is not fully being captured with this simple three-sinusoid model. In future, adding additional terms onto this model may be necessary in order to correct the discrepancy that is still present between model and data. Still, the general conclusion is that the representation of the terdiurnal tide over South Africa in HWM14 does not appear to match the data presented here, indicating the importance of having well-distributed data in construction of such models.

5. Conclusion

We have presented the first results on the nighttime climatology of thermospheric neutral winds over Sutherland, South Africa (i.e., midlatitude region) for an annual period between February 2018 and January 2019. The meridional and zonal winds averaged over Sutherland, South Africa, exhibits a predominantly diurnal variation. A significant semi-annual and terannual variation in the neutral wind averages was not detected.

Overall, the trend of the winds show the expected behavior of a midlatitude site. During local summer months (December-February), the meridional

wind is predominantly equatorward, while the winder months show slower, poleward winds in th early evening. These observations are consistent with stronger heating in the summer hemisphere, and are inline with observations made from other midlatitudes sites (Wu et al., 2019). The peak of the equatorward wind and changes in the wind direction occur much earlier (premidnight) in the summer months compared to winter months (where they occur postmidnight) consistent with other midlatitude (Wu et al., 2019) .

This study also found that the zonal wind velocities are generally eastward during the evening just before midnight, and changed to westward postmidnight through to predawn. The eastward-to-westward transition time in the summer is before midnight (between 01:30 SLT and 02:00 SLT), while the transition occurs much latter in the winter (between 04:00 and 05:30 SLT). Also, the magnitude of zonal wind is between $\sim$ 90 and $\sim$ 120 m/s, consistent with what is obtained from other sectors (e.g., Fejer et al., 2002; Fisher et al., 2015; Kaab et al., 2017).

We see that the model agreement for the zonal wind is particularly poor. The cause of this difference between data and model was investigated and was determined to be the result of a difference in phase shift of the terdiurnal tide. By fitting the diurnal, semidiurnal and terdiurnal tides to the output of HWM and shifting the phase of the terdiurnal tide, we were able to improve the agreement between the model output and the data.

Data availability

The line of sight (LOS) neutral wind from the FPI used in this work is available at http://airglow.ece.illinois.edu/Data/Calendar. The horizontal wind model (HWM14) and NRLMSISE-00 model data were obtained from https://github.com/timduly4/pyglow, using python package while the KP and AP indices as well as $F_{10.7}$ were obtained from https://omniweb.gsfc.nasa.gov/form/dx1.html .

Acknowledgments

The authors would like to thank Brian Harding and Fasil Tesema for their support and meaningful contribution in processing the FPI data. Work at the University of Illinois was supported by the National Science Foundation through grant AGS-16-51298.

References

Bamgboye, D., McClure, J., 1982. Seasonal variation in the occurrence time of the equatorial midnight temperature bulge. Geophysical Research Letters 9(4), 457–460, doi:10.1029/GL009i004p00457.

Brum, C.G.M., Tepley, C.A., Fentzke, J.T., Robles, E., dos Santos, P.T., Gonzalez, S.A., 2012. Long-term changes in the thermospheric neutral winds over arecibo: Climatology based on over three decades of Fabry-Perot observations. Journal of Geophysical Research: Space Physics 117, 117, A00H14, doi:10.1029/2011JA016458.

Chu, K., 2019. Tidal analysis of modeled thermospheric winds to improve agreement with measurements over South Africa. MSc. thesis, University of Illinois at Urbana-Champaign, http://hdl.handle.net/2142/104808.

Drob, D.P., Emmert, J.T., Meriwether, J.W., Makela, J.J., Doornbos, E., Conde, M., Hernandez, G., Noto, J., Zawdie, K.A., McDonald, S.E., et al., 2015. An update to the horizontal wind model (HWM): The quiet time thermosphere. Earth and Space Science 2, 301–319, doi:10.1002/2014EA000089.

Emmert, J., Faivre, M., Hernandez, G., Jarvis, M., Meriwether, J., Niciejewski, R., Sipler, D., Tepley, C., 2006. Climatologies of nighttime upper thermospheric winds measured by ground-based Fabry-Ferot interferometers during geomagnetically quiet conditions: 1. local time, latitudinal, seasonal, and solar cycle dependence. Journal of Geophysical Research: Space Physics 111, A12302, doi:10.1029/2006JA011948.

Emmert, J., Fejer, B.G., Shepherd, G., Solheim, B., 2002. Altitude dependence of middle and low-latitude daytime thermospheric disturbance winds measured by windii. Journal of Geophysical Research: Space Physics 107, (A12), 1483, doi:10.1029/2002JA009646.

Fejer, B.G., Emmert, J., Sipler, D., 2002. Climatology and storm time dependence of nighttime thermospheric neutral winds over Millstone Hill. Journal of Geophysical Research: Space Physics 107, *107*(A5), doi:10.1029/2001JA000300.

Fisher, D.J., Makela, J.J., Meriwether, J.W., Buriti, R.A., Benkhaldoun, Z., Kaab, M., Lagheryeb, A., 2015. Climatologies of nighttime thermospheric

winds and temperatures from Fabry-Perot interferometer measurements: From solar minimum to solar maximum. Journal of Geophysical Research: Space Physics 120, 6679–6693, doi:10.1002/2015JA021170.

Harding, B.J., 2017. Midlatitude thermospheric wind and temperature: networked Fabry-Perot interferometer observations and radiative transfer modeling. Ph.D. thesis. University of Illinois at Urbana-Champaign, http://hdl.handle.net/2142/97286.

Harding, B.J., Gehrels, T.W., Makela, J.J., 2014. Nonlinear regression method for estimating neutral wind and temperature from Fabry–Perot interferometer data. Applied optics 53(4), 666–673, doi:10.1364/AO.53.000666.

Häusler, K., Lühr, H., Rentz, S., Köhler, W., 2007. A statistical analysis of longitudinal dependences of upper thermospheric zonal winds at dip equator latitudes derived from CHAMP. Journal of atmospheric and solar-terrestrial physics 69(12), 1419–1430, doi.org/10.1016/j.jastp.2007.04.004

Heelis, R., 2004. Electrodynamics in the low and middle latitude ionosphere: A tutorial. Journal of Atmospheric and Solar-Terrestrial Physics 66(10), 825–838, doi.org/10.1016/j.jastp.2004.01.034.

Jiang, G., Xu, J., Wang, W., Yuan, W., Zhang, S., Yu, T., Zhang, X., Huang, C., Kerr, R.B., Noto, J., et al., 2018. A comparison of quiet time thermospheric winds between FPI observations and model calculations. Journal of Geophysical Research: Space Physics 123, 7789–7805, doi.org/10.1029/2018JA025424.

Kaab, M., Benkhaldoun, Z., Fisher, D.J., Harding, B., Bounhir, A., Makela, J.J., Laghriyeb, A., Malki, K., Daassou, A., Lazrek, M., 2017. Climatology of thermospheric neutral winds over Oukaïmeden observatory in Morocco. Ann. Geophys 35, 161–170, doi.org/10.5194/angeo-35-161-2017.

Link, R., Cogger, L., 1988. A reexamination of the oi 6300-å nightglow,. Journal of Geophysical Research: Space Physics 93, 93(A9)9883–9892.

Makela, J.J., Fisher, D.J., Meriwether, J.W., Buriti, R.A., Medeiros, A.F., 2013. Near-continual ground-based nighttime observations of thermospheric neutral winds and temperatures over equatorial Brazil from 2009

to 2012. Journal of Atmospheric and Solar-Terrestrial Physics 103, 94–102, doi.org/10.1016/j.jastp.2012.11.019.

McLandress, C., Shepherd, G.G., Solheim, B.H., 1996. Satellite observations of thermospheric tides: Results from the wind imaging interferometer on UARS. Journal of Geophysical Research: Atmospheres 101, 101(D2)4093–4114,doi:10.1029/95JD03359

Meriwether, J., 2006. Studies of thermospheric dynamics with a Fabry–Perot interferometer network: A review. Journal of Atmospheric and Solar-Terrestrial Physics 68, 68(13), 1576–1589, doi.org/10.1016/j.jastp.2005.11.014.

Rees, D., 1995. Observations and modelling of ionospheric and thermospheric disturbances during major geomagnetic storms: A review. Journal of Atmospheric and Terrestrial Physics 57, (12)1433–1457, doi.org/10.1016/0021-9169(94)00142-B.

Sahai, Y., Takahashi, H., Fagundes, P., Clemesha, B., Teixeira, N., Bittencourt, J., 1992. Observations of thermospheric neutral winds at 23^0S. Planetary and Space Science 40, 40(6), 767–773, doi.org/10.1016/0032-0633(92)90105-W.

Sivla, W., Ogunjobi, O., Okoro, E., Ugonabo, O., Orji, P., 2019. Thermospheric neutral winds over Abuja, Nigeria .*International Journal of Physical Sciences*, *14*(2), 15–20, doi.org/10.5897/IJPS2018.4773.

Spencer, N., Wharton, L., Carignan, G., Maurer, J., 1982. Thermosphere zonal winds, vertical motions and temperature as measured from dynamics explorer. Geophysical Research Letters 9, 953–956, doi:10.1029/GL009i009p00953.

Taylor, K.E., 2001. Summarizing multiple aspects of model performance in a single diagram. Journal of Geophysical Research: Atmospheres 106, (D7)7183–7192, doi:10.1029/2000JD900719

Tesema, F., Mesquita, R., Meriwether, J., Damtie, B., Nigussie, M., Makela, J., Fisher, D., Harding, B., Yizengaw, E., Sanders, S., 2017. New results on equatorial thermospheric winds and temperatures from Ethiopia, Africa. Annales Geophysicae 35(333-344), doi.org/10.5194/angeo-35-333-2017.

Wu, Q., Sheng, C., Wang, W., Noto, J., Kerr, R., McCarthy, M., Huang, C., Zhang, X., Sarris, T., 2019. The midlatitude thermospheric dynamics from an interhemispheric perspective. Journal of Geophysical Research: Space Physics 124, 7971–7983, doi.org/10.1029/2019JA026967.

Xu, H., Shiokawa, K., Oyama, S.i., Nozawa, S., 2019. High-latitude thermospheric wind study using a Fabry–Perot interferometer at Tromsø in Norway: averages and variations during quiet times. Earth, Planets and Space 71, 110, doi.org/10.1186/s40623-019-1093-8.

Yu, T., Huang, C., Zhao, G., Mao, T., Wang, Y., Zeng, Z., Wang, J., Xia, C., 2014. A preliminary study of thermosphere and mesosphere wind observed by Fabry-Perot over Kelan, China. Journal of Geophysical Research: Space Physics 119, 4981–4997, doi:10.1002/2013JA019492.

Table 1: An improvements(D) from shifting terdiurnal tide for each month.

Months	Improvements (D)
Feb	1.82
Mar	14.09
Apr	14.19
May	6.81
Jun	6.62
Jul	12.95
Aug	1.82
Sep	21.76
Oct	15.46
Nov	23.03
Dec	25.59
Jan	7.49

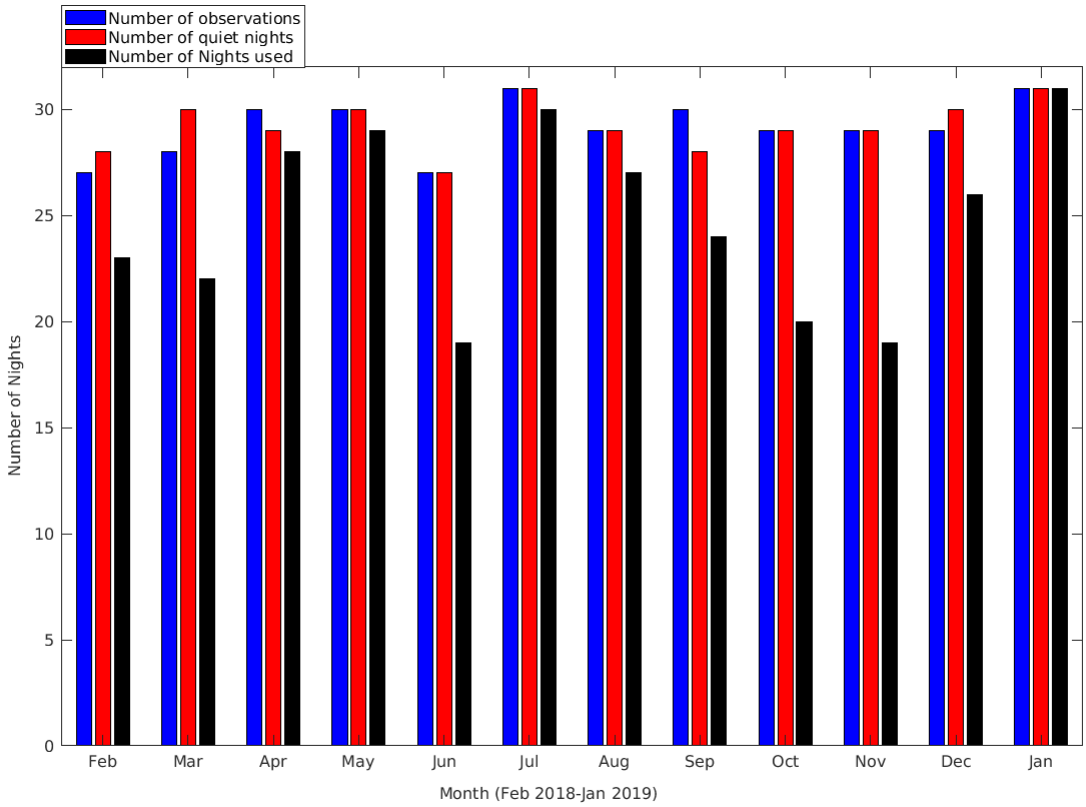

Figure 1: The number of nights observation, the number of quiet nights, and the number of used nights per month from February 2018 to January 2019.

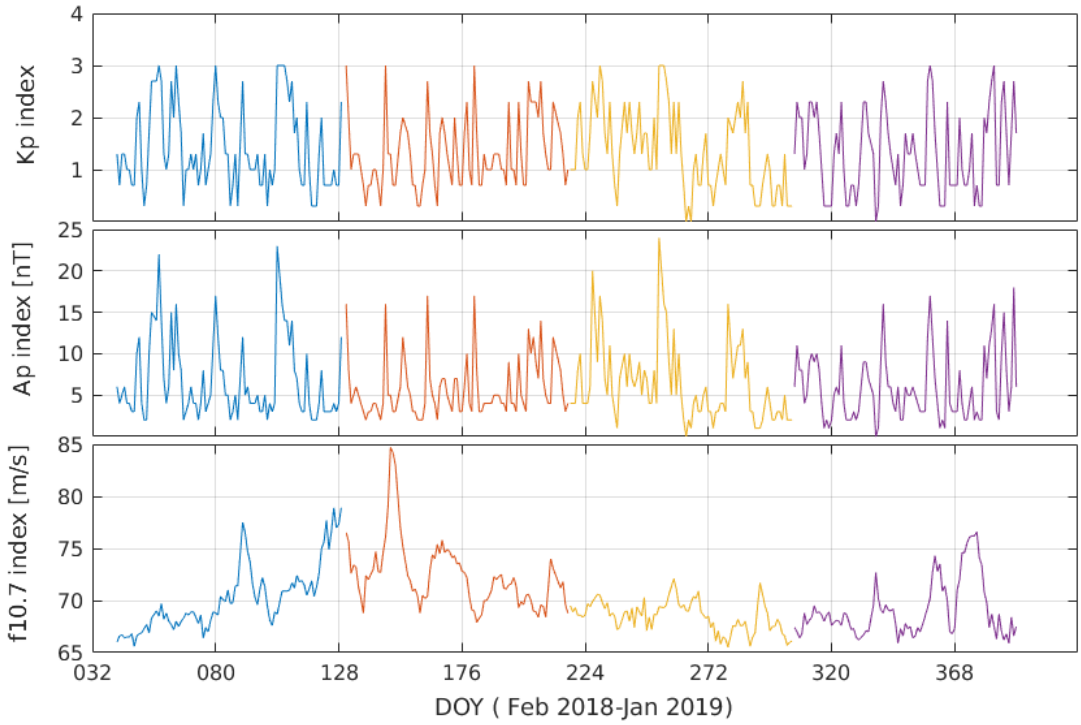

Figure 2: The seasonal occurrence of the Kp (top row), Ap index (middle row) and solar flux (third row) blue, red, yellow and indigo represent Autum, Winter, Spring, Summer, respectively.

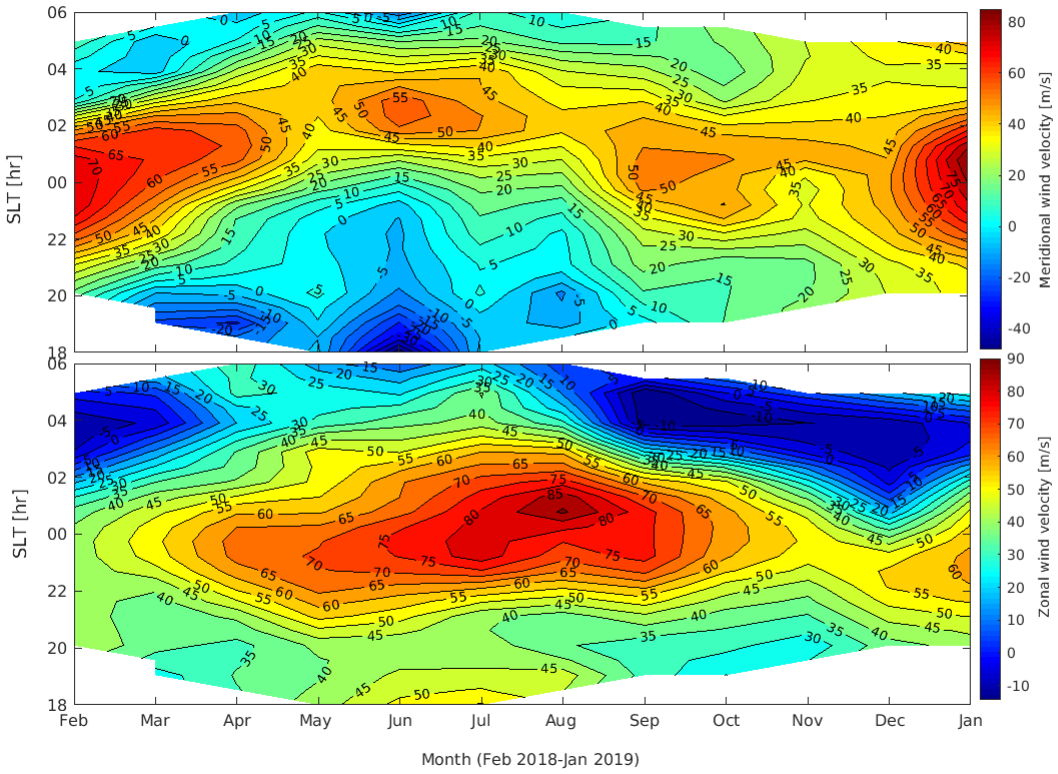

Figure 3: Contour plots of the monthly-averaged meridional wind (top) and zonal wind (bottom) measured by the FPI.

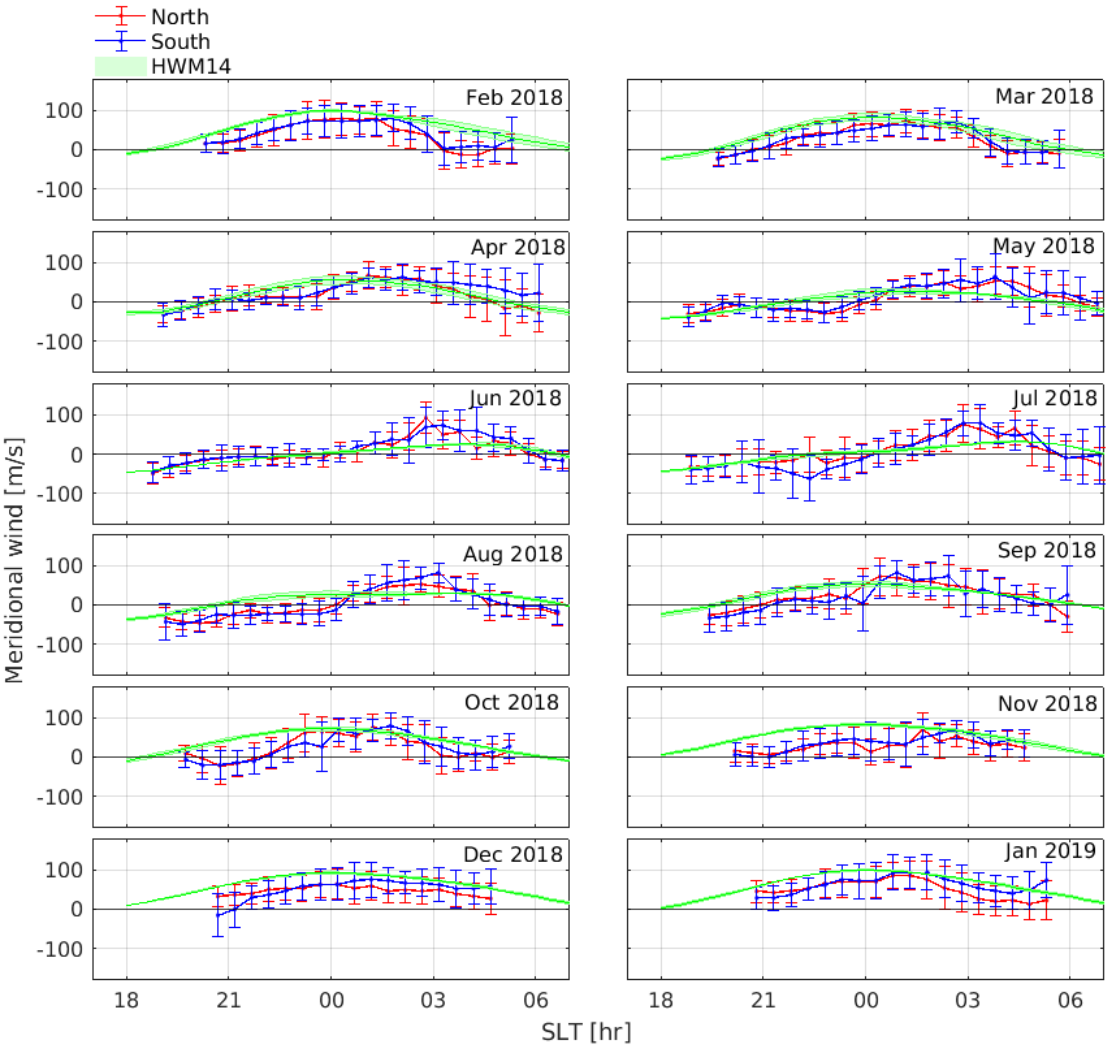

Figure 4: Monthly-averaged meridional wind measured by the FPI (red and blue) and predicted by HWM14 (green) between February 2018 and January 2019. Wind value below "0" is polewards (negative) and above "0" is equatorwards (positive). The error bars indicate standard deviation in the measurements while thickness in the HWM14 represents the range of variability.

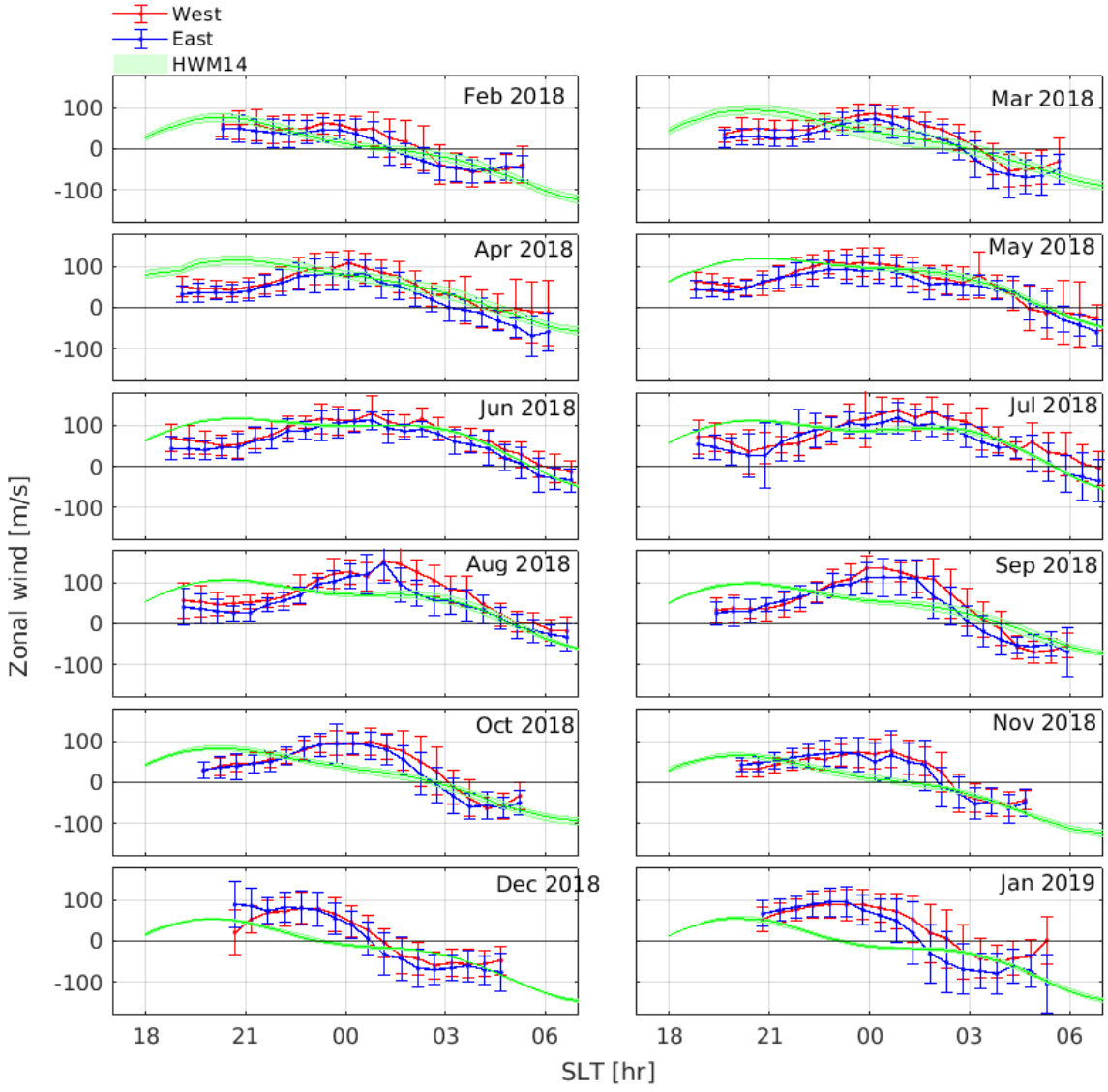

Figure 5: Monthly-averaged zonal wind (red and blue FPI, and green HWM14) between February 2018 and January 2019. Wind value below "0" is westward (negative) and above "0" is eastward (positive).

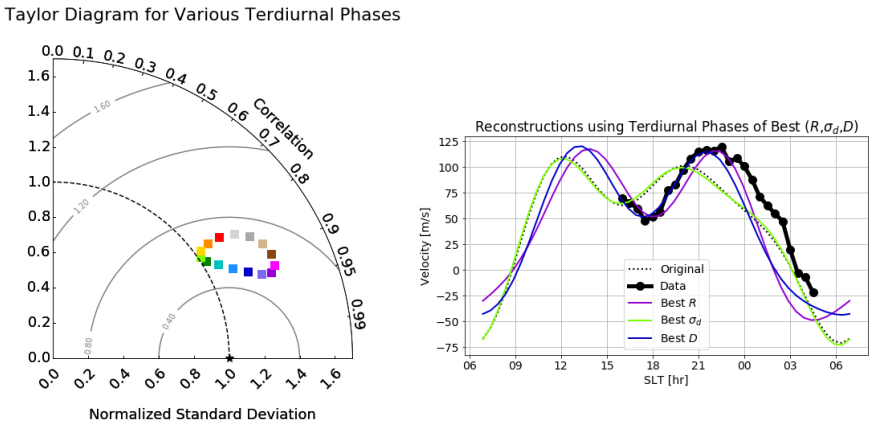

(a)

(b)

Figure 6: Taylor diagram for various terdiurnal phases (left) and the reconstructions (right) corresponding to the best R_d (purple), σ_d (green) and D(blue) for February 2018.

Figure 7: Results obtained by introducing a phase shift to the terdiurnal component in the HWM14 zonal winds. The original modeled winds (blue) are seen to agree better with the data (red) after this shift is introduced (green).